Synchronous Chlorophyll-a and Sea Surface Salinity Variability in the Equatorial Pacific Ocean

Wei Shi and Menghua Wang

***Abstract*—Using chlorophyll-a (Chl-a) concentration data derived from the Visible Infrared Imaging Radiometer Suite onboard the Suomi National Polar-orbiting Partnership, the *in situ* measurements from the tropical ocean atmosphere moorings, and the sea surface salinity (SSS) data from the Soil Moisture Active Passive mission and Aquarius satellite, we report synchronous Chl-a and SSS variability in the Equatorial Pacific Ocean on the daily and monthly bases. During the El Niño event in 2015, a decrease in Chl-a and SSS occurred and developed within the same timeframe, and possessed similar spatial patterns across the Equatorial Pacific Ocean. Enhanced Chl-a and SSS coincided and colocated (in timing, location, spatial coverage, and extent) during the La Niña event in 2020. In contrast, sea surface temperature variability did not relate to Chl-a and SSS variability across the Equatorial Pacific Ocean. Chl-a and SSS were found to covary on the daily basis driven by the tropical instability waves. The mechanism that caused the synchronous Chl-a and SSS variability in the Equatorial Pacific Ocean on both the daily and monthly bases is addressed and discussed.**

***Index Terms*—Biological activity, chlorophyll-a variability, El Niño Southern Oscillation (ENSO), Equatorial Pacific Ocean, sea surface salinity (SSS), sea surface temperature (SST), tropical atmosphere ocean (TAO).**

I. Introduction

THE ocean and atmosphere processes and dynamics in the Equatorial Pacific Ocean (see Fig. 1) have significant effects on the global climate and oceans [1], [2]. The climate fluctuation known as El Niño Southern Oscillation (ENSO) reoccurs every couple of years [3]. During the warm phase (El Niño) of ENSO, the anomalous warming sea surface temperature (SST) dominates in either the eastern Equatorial Pacific Ocean (EP-El Niño) or the central Equatorial Pacific Ocean (CP-El Niño). The CP-El Niño becomes more frequent than the EP-El Niño due to global warming driven by anthropogenic climate change [4]. On the other hand, during the cold phase (La Niña) of ENSO, La Niña is associated with intensified trade winds and low SSTs in the Equatorial Pacific Ocean [5], [6].

Manuscript received 7 September 2022; revised 2 February 2023; accepted 3 March 2023. Date of publication 10 March 2023; date of current version 24 March 2023. This work was supported by the Joint Polar Satellite System funding. *(Corresponding author: Wei Shi.)*

Wei Shi is with the Center for Satellite Applications and Research, NOAA/NESDIS, College Park, MD 20746 USA, and also with the Cooperative Institute for Research in the Atmosphere, Fort Collins, CO 80521 USA (e-mail: wei.1.shi@noaa.gov).

Menghua Wang is with the Center for Satellite Applications and Research, NOAA/NESDIS, College Park, MD 20740 USA (e-mail: menghua.wang@noaa.gov).

Digital Object Identifier 10.1109/JSTARS.2023.3255179

As the single most significant interannual ocean-atmosphere process, ENSO variability in the Equatorial Pacific Ocean modulates weather and climate anomalies [5], [7], [8], [9], affects global carbon cycle [10], [11], [12], and drives changes of the terrestrial and marine ecosystem [13], [14], [15]. In fact, ENSO impacts on agricultural, economic, and societal issues are also enormous [16], [17], [18].

In the Equatorial Pacific Ocean, the ocean's physical, biological, and biogeochemical variabilities are closely linked to the ENSO event. Conversely, the changes in these physical and biological parameters, such as SST and chlorophyll-a (Chl-a), which are driven by the ENSO cycle, can also provide possible feedback to ENSO [19], [20]. The oceanic phytoplankton in the tropics rapidly responds to EP-El Niño and CP-El Niño [21]. Indeed, the ocean's primary productivity in the Equatorial Pacific Ocean exhibited substantial changes in response to a major El Niño to La Niña transition between September 1997 and August 2000 [22]. During the 1997–1998 El Niño, the Equatorial Pacific Ocean experienced significant variations in chemical and biological activities. Specifically, it became nutrient-impoverished, and Chl-a was at a record low [23].

The chemical and biological perturbations are coupled with physical processes in the Equatorial Pacific Ocean [24]. However, the spatial patterns of the enhanced (decreased) Chl-a and anomalously low (high) SST do not synoptically match up during La Niña and El Niño [25], [26]. The biological responses are highly disparate along the equator, and are attributed to different driving mechanisms. The Chl-a anomaly and the 20°C isotherm depth anomaly are moderately related in the western Equatorial Pacific Ocean, and they become unrelated in the central and central-eastern Equatorial Pacific Ocean [24], [26].

As one of the most important physical parameters, sea surface salinity (SSS) also plays a critical role and shows high variability in the El Niño and La Niña events. Large SSS differences associated with El Niño are confined to the fresh pool and Niño 3.4 (5°N–5°S, 170°W–120°W) regions during CP- and EP-El Niño events [27]. The western Pacific Warm Pool has significantly warmed and freshened since the middle of last century [28]. The central Pacific type of El Niño and the eastern Pacific El Niño show contrasting SSS distributions in the Equatorial Pacific Ocean [29]. The SSS variability was influenced by both the advective processes and evaporation minus precipitation (E-P) variability during the 1997–1998, 2012–2013, and 2014–2015 ENSO events [30]. In fact, salinity played a critical role in the 2014/2015 failed El Niño [31]. The ENSO intensity and asymmetry were also found to be affected by the zonal structure

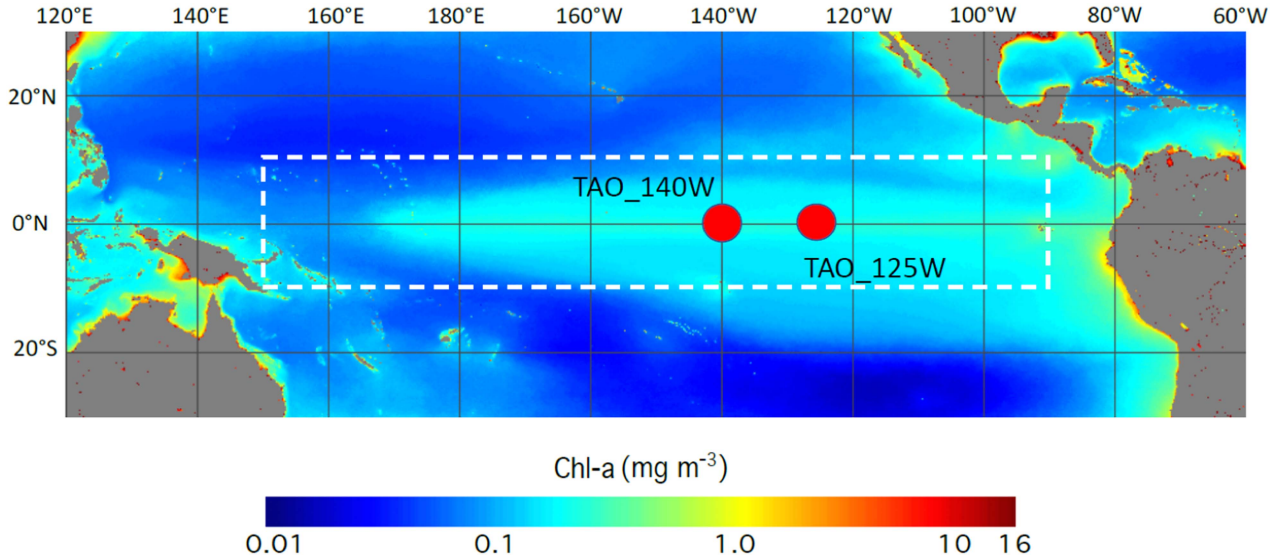

Fig. 1. VIIRS-SNPP-derived climatology Chl-a in the Equatorial Pacific Ocean with the study region marked by a white dashed box. The locations of the TAO_140W mooring at [140°W, 0°N] and TAO_125W mooring at [125°W, 0°N] are also noted for further data analysis.

of tropical Pacific SSS anomalies [32]. Indeed, a recent study shows that the tropical instability wave (TIW) not only drives the SSS variability, but also the Chl-a variability in the central and central-eastern Equatorial Pacific Ocean [33].

Satellite observations have long been used as the major tools to study large-scale ocean phenomena and ocean processes via corresponding products, such as SST, Chl-a, SSS, and sea surface height. Due to the lengthy history of these satellite-derived products, the ocean physical, biological, and biogeochemical processes and their interactions in the Equatorial Pacific Ocean have been extensively studied and explored. Even though satellite-derived SSS became available after the 2000s, they have already been used in various studies.

In the Equatorial Pacific Ocean region, the TIW impact on the SSS from observations of the NASA Aquarius satellite was observed [34]. The SSS from the Soil Moisture Ocean Salinity (SMOS) satellite mission revealed the northward advection of the surface water across the tropical North Pacific Ocean [35]. The SSS signature during the 2010–2011 La Niña was also reported by SMOS observations [36]. Research also shows that satellite-SSS observations from Aquarius, SMOS, etc., can improve the coupled ENSO forecasts [37], [38]. The 33-day and 17-day TIW cycles were also detected in the Equatorial Pacific Ocean from the SMOS observations [39].

In the Equatorial Pacific Ocean, satellite observations already showed that the anomalous pattern of Chl-a does not match with SST synoptically [23], [25], [26]. This suggests that the anomalous SST do not covary with Chl-a anomalies, and the driving forces for SST and Chl-a dynamics are not exactly the same. However, no research has been conducted about the change and variation in SSS and Chl-a in the Equatorial Pacific Ocean. The objective of this study is to use available satellite SSS and Chl-a data, as well as *in situ* measurements, to assess the linkage between the SSS and Chl-a variability, and to further explore the driving mechanism for this phenomenon in the Equatorial Pacific Ocean. In this study, we analyze multiyear observations of Chl-a from the Visible Infrared Imaging Radiometer Suite (VIIRS) onboard the Suomi National Polar-orbiting Partnership (SNPP), and SSS from Aquarius and Soil Moisture Active Passive (SMAP) missions in the Equatorial Pacific Ocean. We also compare daily SSS observations at the tropical ocean atmosphere (TAO) moored buoy arrays and VIIRS-measured daily gap-free Chl-a data [40], [41], [42]. The dynamics and covariation of SSS and Chl-a in the Equatorial Pacific Ocean on both the daily and interannual bases are investigated, and the mechanism that leads to the synchronous changes of SSS and Chl-a is also discussed and addressed.

II. Data and Method

A. Chl-a Product From VIIRS Observations

VIIRS-SNPP is the continuation mission for satellite ocean color observations following the Sea-Viewing Wide Field-of-View Sensor [43] and the Moderate Resolution Imaging Spectroradiometer [44]. VIIRS-SNPP has been providing high quality global Chl-a products since 2012 [45], [46]. The ocean color index (OCI) Chl-a algorithm [47] is used to generate Chl-a products for the global ocean and inland waters.

Because satellite-derived Chl-a data are often not available over large regions due to limitations, such as cloud coverage, sun glint contamination, etc. [48], the Data Interpolating Empirical Orthogonal Functions (DINEOF) method was developed to produce a gap-free daily global Chl-a product from VIIRS observations, which have an accuracy similar to the original data [40], [41]. In this work, both the monthly composite Chl-a and daily DINEOF Chl-a products [40] are used to study the daily, seasonal, and interannual variability along with their relations to the corresponding SSS variability in daily and monthly scales.

B. SSS Data From Aquarius and SMAP Measurements

Aquarius [49] was the first instrument in the US to measure SSS onboard the Argentine SAC-D spacecraft. It provided satellite SSS measurements between the mid-2011 and mid-2015 with an instrument spatial resolution of 150 km and a repeat cycle of seven days. The SSS accuracy from Aquarius is about 0.2 psu [50].

Launched in early 2015, SMAP provides observations of global soil moisture. It also provides SSS observations for the global ocean using the onboard radar and radiometer [51], [52]. The SMAP orbits at an altitude of 685 km and has an 8-day repeat cycle. The SSS measurements obtained by the SMAP mission are based on L-band microwave sensitivity to water salinity. Thus, SSS can be retrieved from SMAP radiometer measurements [53]. Since April 2015, SMAP has provided global ocean SSS observations. The SMAP spatial resolutions are on a 25-km swath grid for Level-2B data and on $0.25° \times 0.25°$ for Level-3 data. The validation of SMAP SSS shows that it has $\sim$0.2 psu accuracy on a monthly basis in the tropics compared to the objectively interpolated gridded monthly Argo datasets, and it can track large salinity changes occurring within a month that remain consistent with those changes measured from buoys [54].

The SSS measurements from Aquarius and SMAP provide us an opportunity to study the decade-long SSS variability for the global ocean in both the meso-scale and the synoptic-scale. In this study, the daily 8-day-runing-mean and monthly SSS measurements from Aquarius and SMAP are used to characterize and quantify the SSS variability and its covariation with Chl-a changes in the Equatorial Pacific Ocean. Our evaluation of the overlapped Aquarius and SMAP SSS in April and May 2015 shows that the SSS difference between Aquarius and SMAP is insignificant. In fact, the mean and median differences from these two datasets during these two months are 0.013 and 0.014 psu, respectively, for the global ocean. This provides evidence that Aquarius SSS and SMAP SSS are consistent and they can be fused together to study SSS variability between 2011 and 2021 in the Equatorial Pacific Ocean.

In this work, the monthly Aquarius and SMAP SSS in the Equatorial Pacific Ocean were acquired to quantify the synoptic variability of SSS and to examine whether SSS variations covary with those of Chl-a. The SMAP daily SSS (with the 8-day-running-mean) are used to characterize the SSS variability on the daily basis, and are compared to the corresponding daily Chl-a variability in the Equatorial Pacific Ocean.

C. SSS Measurements at TAO Moored Buoy Arrays

Aquarius and SMAP can provide SSS measurements in the Equatorial Pacific Ocean with coarse spatial and temporal resolutions. To understand SSS variability and its correlation with the Chl-a change on the daily basis, the *in situ* daily measurements of SSS at the TAO arrays are acquired (https://www.pmel.noaa.gov/gtmba/pmel-theme/pacific-ocean-tao). The TAO buoys were set up across the Equatorial Pacific Ocean to better understand and predict climate variations related to the ENSO events with multinational efforts [55]. A variety of the ocean and atmospheric parameters, such as ocean temperature and salinity profiles, wind speed and direction, air temperature, current, and long-wave radiation, were measured on the daily basis. In this study, we use SSS measurements taken at the locations [140°W, 0°N] and [125°W, 0°N] in 2019 and 2020 to investigate short-term SSS variation, and to explore whether its variation is in phase with that of Chl-a on the daily basis.

D. Chl-a and SSS Anomalies

In the Equatorial Pacific Ocean, both Chl-a and SSS have significant seasonal variability. To study Chl-a and SSS anomalies and their interannual variability in response to the ENSO activity, the monthly climatology Chl-a were computed from VIIRS-SNPP observations between February 2012 and August 2021. Similarly, the monthly climatology SSS were calculated from the Aquarius and SMAP observations between February 2012 and August 2021. The climatology monthly Chl-a and SSS were removed from the corresponding monthly data to derive the time series of Chl-a and SSS anomalies in the Equatorial Pacific Ocean.

III. Results and Discussion

A. Chl-a Anomaly Ratio and SSS Anomaly During the ENSO Event

In the period between 2012 and 2021, the Equatorial Pacific Ocean experienced a significant El Niño event in 2015 and La Niña event in 2020 as defined by the multivariate ENSO index (MEI) [56], [57] (https://psl.noaa.gov/enso/mei/). Specifically, the MEI values were –1.9 and +1.0 in December 2015 (El Niño event) and August 2020 (La Niña event), respectively. These two months will be used as examples to compare the spatial patterns in the Chl-a anomaly ratio with those from the SSS anomaly in various ENSO phases in the region. It is noted that the Chl-a anomaly ratio is computed as a relative difference (i.e., Chl-a ratio between the monthly Chl-a and its corresponding monthly climatology Chl-a), whereas the SSS anomaly is calculated as a difference with respect to the corresponding climatology value. It is more appropriate and sensitive to use a Chl-a relative difference for low Chl-a values [58].

In December 2015, the coverage of enhanced Chl-a with Chl-a > 0.2 mg/m^3 was much smaller than that of enhanced Chl-a in the climatology Chl-a for the same month. The enhanced Chl-a can be found stretching from 150°W to the eastern Equatorial Pacific Ocean [see Fig. 2(a)]. In comparison, the enhanced Chl-a can be found much further to the west covering a wide swath from 180° to 90°W [see Fig. 2(c)]. The SSS spatial patterns [see Fig. 2(b) and (d)] are different from those of Chl-a. Relatively higher SSS in the southern Equatorial Pacific Ocean were found as compared to SSS in the northern Equatorial Pacific Ocean. There were no enhanced SSS along the equator for both SSS in December 2015 [see Fig. 2(b)] and the climatology SSS in December [see Fig. 2(d)] in comparison to the SSS in the region off the Equatorial Pacific Ocean. In December 2015, the region with SSS over $\sim$35.5 psu only covered the southern Equatorial Pacific Ocean to the east of 160°W, whereas climatology SSS in

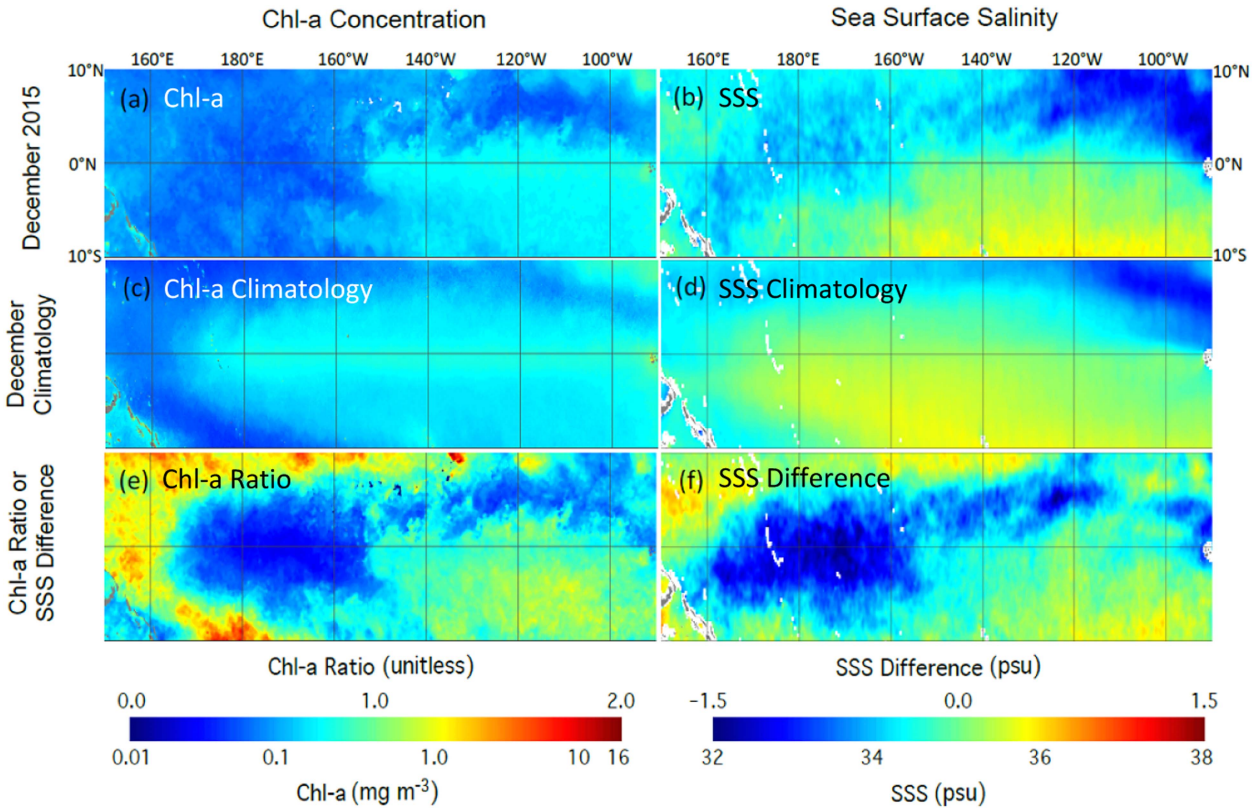

Fig. 2. Comparisons of Chl-a and SSS spatial distributions (and their variations) in the Equatorial Pacific Ocean during the El Niño event (December 2015) for panels of (a) Chl-a, (c) corresponding climatology Chl-a in December, and (e) Chl-a anomaly ratio; and (b) SSS, (d) corresponding climatology SSS in December, and (f) SSS difference. Note that the same color bar is used for Chl-a, Chl-a ratio, SSS, and SSS difference with different scales.

December stretched to the west of the 180° and reached north of the equator [see Fig. 2(d)].

Even though the spatial patterns of Chl-a and SSS are quite different from their observations in December 2015 and their corresponding December climatology, the spatial variability of the Chl-a anomaly ratio in terms of the ratio between Chl-a in December 2015 and the corresponding Chl-a climatology in December [see Fig. 2(e)] was analogous to the spatial pattern of the SSS anomaly, which was calculated as the difference between the SSS in December 2015 and the corresponding SSS climatology in December [see Fig. 2(f)]. Specifically, the Chl-a ratio in the central Equatorial Pacific Ocean between 165°E–155°W dropped to less than 0.5 [see Fig. 2(e)]. In this region, the SSS anomalies reached below –1.0 psu [see Fig. 2(f)]. Similarly, the decreased/enhanced Chl-a in the vast area eastward from 140°W in the Equatorial Pacific Ocean were also colocated with the decreased/enhanced (negative/positive) SSS. Thus, the location, coverage, and the magnitude of the low/high Chl-a ratio synoptically matched with those of the SSS anomaly in December 2015 during the El Niño event.

During the La Niña event in August 2020, both Chl-a and SSS showed different variations in comparison to the changes during the El Niño event. Higher Chl-a [see Fig. 3(a)] and SSS [see Fig. 3(b)] could be observed further westward and further off the equator when placed in juxtaposition to the climatology Chl-a [see Fig. 3(c)] and SSS [see Fig. 3(d)] in the same month. In the western Equatorial Pacific Ocean, a notable increase in Chl-a and SSS could be observed in August 2020 when set against the climatology Chl-a and SSS in the same month. At the equator in the western Equatorial Pacific Ocean, Chl-a increased from ∼0.1 mg/m^3 of the climatology value to over ∼0.3 mg/m^3 in August 2020, whereas SSS increased from climatology ∼35 psu to over ∼35.5 psu.

The spatial pattern of the Chl-a anomaly ratio in Fig. 3(e) matched well with the SSS anomaly synoptically in August 2020 [see Fig. 3(f)]. The enhanced Chl-a in Fig. 3(e) in the western Equatorial Pacific Ocean were generally colocated with the positive SSS anomaly in Fig. 3(f), and the magnitude of the enhancement of Chl-a was also consistent with the strength of the SSS anomaly. It is also noted that the scattered pattern of the higher Chl-a anomaly ratio in the northern Equatorial Pacific Ocean was also seen in the positive SSS anomaly [see Fig. 3(f)]. In the region eastward from 160°W along the equator, the Chl-a ratio was close to 1.0 [see Fig. 3(e)]. In comparison, the corresponding SSS anomaly in August 2020 was close to 0 psu.

The maps of the Chl-a anomaly ratio and SSS anomaly during El Niño in 2015 and La Niña in 2020 show that they had similar synoptic spatial distributions in the Equatorial Pacific Ocean when the ENSO event occurred and resulted in contrasting physical and biological changes. This suggests that the Chl-a change covaried with the SSS change during the ENSO event in

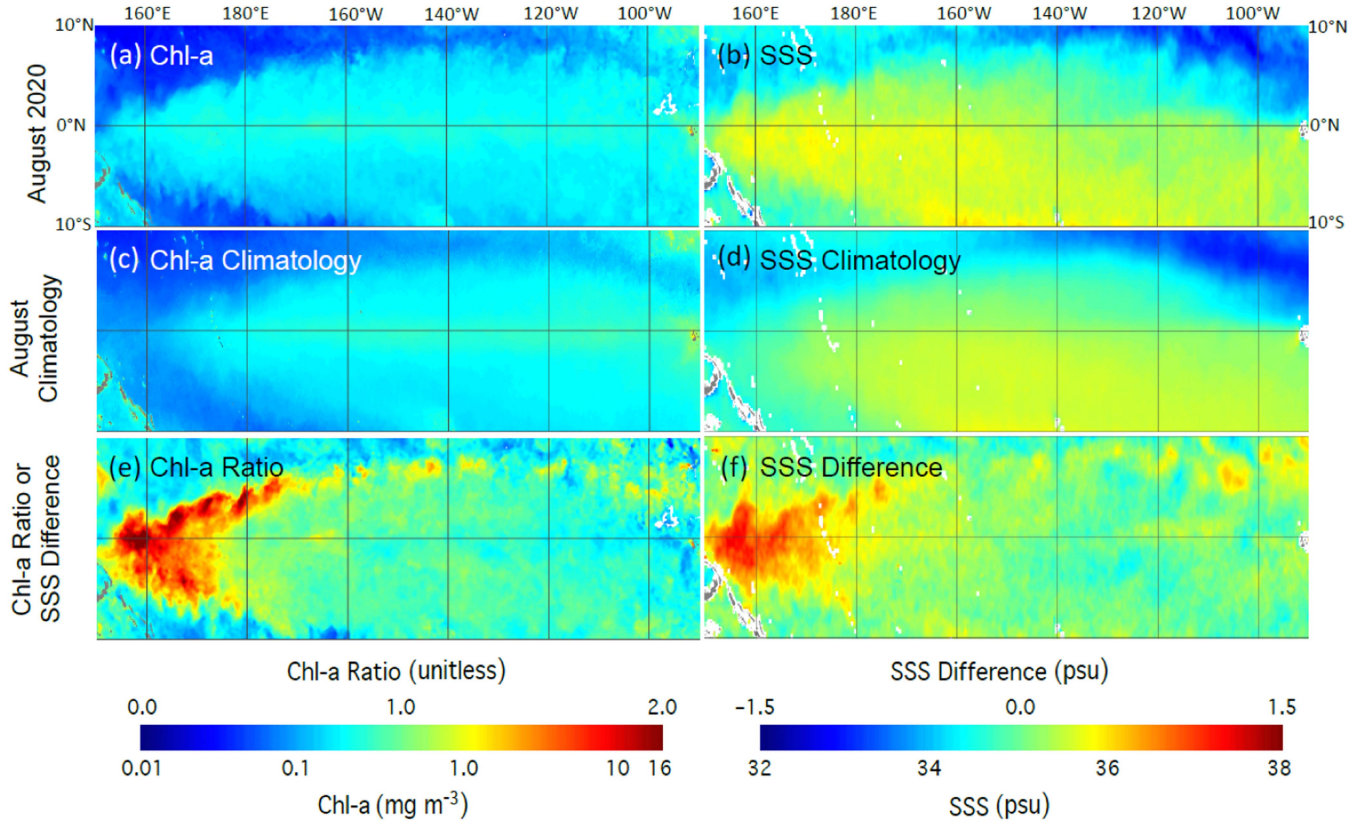

Fig. 3. Comparisons of Chl-a and SSS spatial distributions (and their variations) in the Equatorial Pacific Ocean during the La Niña event (August 2020) for panels of (a) Chl-a, (c) corresponding climatology Chl-a in August, and (e) Chl-a anomaly ratio; and (b) SSS, (d) corresponding climatology SSS in August, and (f) SSS difference. Note that the same color bar is used for Chl-a, Chl-a ratio, SSS, and SSS difference with different scales.

the Equatorial Pacific Ocean. However, the spatial patterns of the Chl-a anomaly ratio and SSS anomaly were apparently different from the corresponding SST anomaly maps in the region in December 2015 for the El Niño event [see Fig. 4(e)] and in August 2020 for the La Niña event [see Fig. 4(f)].

B. Temporal Variations of Chl-a and SSS Anomalies at the Equator

Figs. 2 and 3 show that the Chl-a anomaly ratio is consistent with the SSS anomaly in the spatial domain. To further examine whether the Chl-a anomaly ratio variability also covaried with the SSS anomaly in the temporal domain in the Equatorial Pacific Ocean, the monthly Chl-a anomaly ratio and SSS anomaly variabilities were computed. Fig. 5(a) shows Chl-a anomaly ratio variability at the equator in the period between February 2012 and August 2021, whereas Fig. 5(b) illustrates the SSS anomaly variability at the equator during the same period.

Chl-a anomaly ratio variability [see Fig. 5(a)] and SSS anomaly variability [see Fig. 5(b)] are virtually consistent with each other for both the timing and coverage of the anomalous Chl-a and SSS. During the 2015 El Niño event, anomalously low Chl-a [see Fig. 5(a)] and SSS [see Fig. 5(b)] occurred from April–May 2015, after which they further extended eastward reaching 150°W in late 2015 and early 2016. The anomalously low Chl-a and SSS were back to normal conditions when the El Niño faded in the boreal spring of 2016.

During the period between 2016 and early 2020, the ENSO activities were weak. The notable Chl-a and SSS anomalies were mostly located in the western Equatorial Pacific Ocean to the west of 180°. In the central and eastern Equatorial Pacific Ocean, both Chl-a and SSS anomalies were insignificant in this period. In the western Equatorial Pacific Ocean, the change of the Chl-a anomaly ratio matched with the change of the SSS anomaly in terms of both the timing and stretched area in this period. Specifically, both Chl-a and SSS anomalies were enhanced in the western Equatorial Pacific Ocean when the MEI values were negative between 2016 and 2018, whereas Chl-a and SSS anomalies were both low when the MEI value became positive between 2018 and 2020.

In mid-2020, La Niña started with the MEI value dropped below –1.0. As shown in Fig. 3, enhanced Chl-a and SSS anomalies were observed in the western Equatorial Pacific Ocean. Fig. 5 shows that both the enhanced Chl-a and SSS anomalies were consistent with the progress of La Niña activity. In comparison with the coverage of lower Chl-a and SSS anomalies, higher Chl-a and SSS anomalies were confined to the western Equatorial Pacific Ocean during the 2015 El Niño event. Specifically, the Chl-a anomaly ratio reached over 2.0 and SSS anomaly was over +1.0 psu in late 2020. In the central and eastern Equatorial Pacific Ocean, both Chl-a and SSS anomalies were

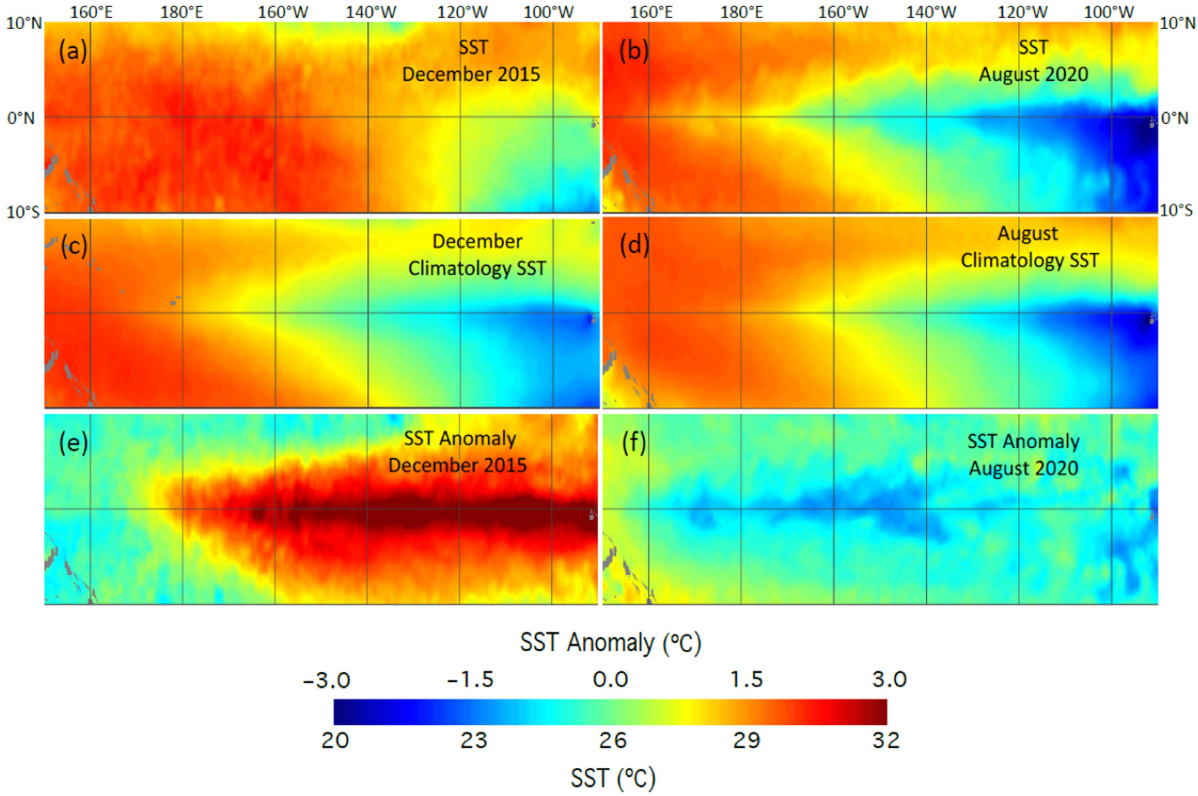

Fig. 4. Comparisons of SST spatial distributions and its variations during the El Niño and La Niña events in the Equatorial Pacific Ocean for panels of (a) SST in December 2015, (c) corresponding climatology SST in December, and (e) SST anomaly in December 2015; and (b) SST in August 2020, (d) corresponding climatology SST in August, and (f) SST anomaly in August 2020.

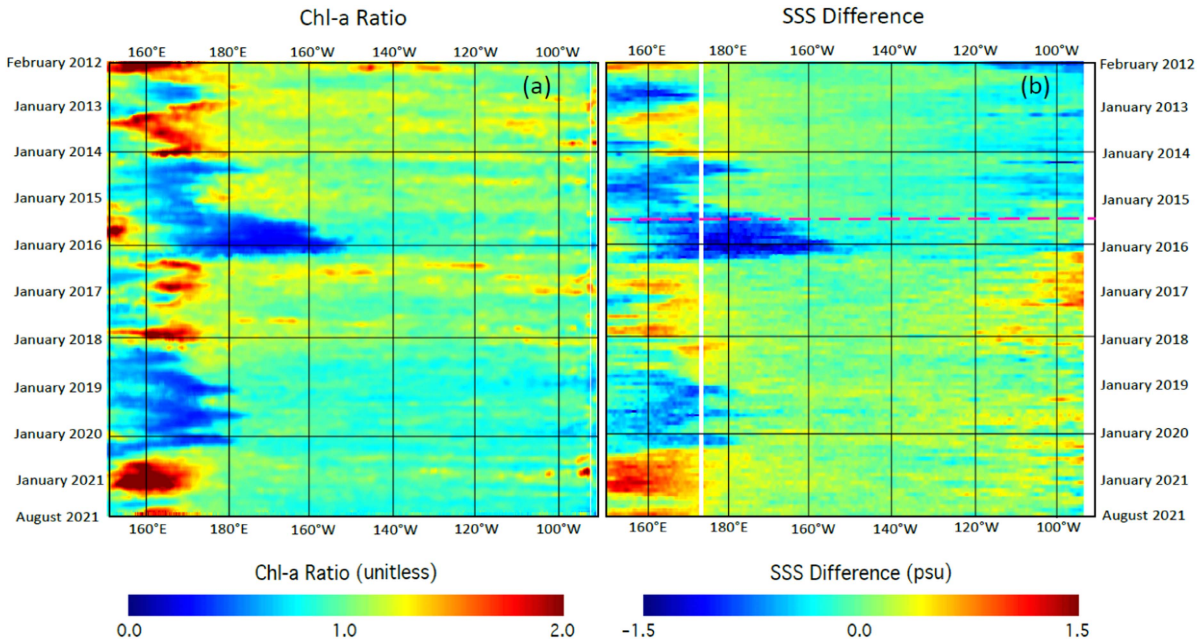

Fig. 5. (a) Longitudinal-temporal section of VIIRS-measured Chl-a anomaly ratio at the equator between February 2012 and August 2021 and (b) longitudinal-temporal section of Aquarius and SMAP-measured SSS anomaly (SSS difference) at the equator between February 2012 and August 2021. Note that the pink line in panel (b) represents the separation of SSS measurements from Aquarius and SMAP.

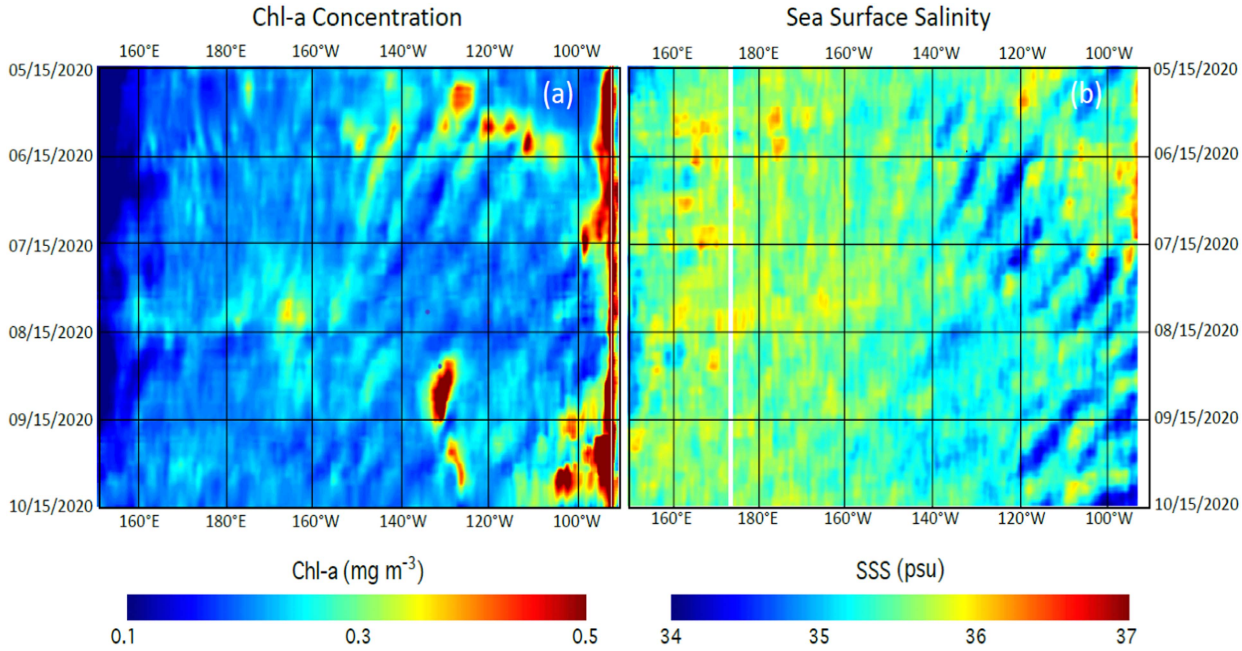

Fig. 6. (a) Longitudinal-temporal section of VIIRS-measured Chl-a at the equator from May 15–October 15, 2020 and (b) longitudinal-temporal section of SMAP-measured SSS at the equator in the same period. The westward propagation features in panels (a) and (b) are caused by the TIWs.

insignificant during this La Niña event. This is different from the SST anomaly, as shown in Fig. 4(f).

C. Chl-a and SSS Variations on the Daily Basis

Figs. 2, 3, and 5 show that the Chl-a anomaly ratio and SSS anomaly changes were in phase synoptically on the monthly scales following the ENSO activities in the Equatorial Pacific Ocean. To study the Chl-a and SSS variations on the daily basis, the daily DINEOF Chl-a and daily 8-day-running-mean SSS were examined. Using the period between May 15–October 15, 2020, as an example, Fig. 6 shows the Chl-a variation [see Fig. 6(a)] and the SSS variation [see Fig. 6(b)] across the equator. Fig. 6(a) and (b) clearly shows the impact of the westward propagating TIW on Chl-a and the SSS in the eastern Equatorial Pacific Ocean of 160°W. Specifically, the TIW caused Chl-a and SSS highs simultaneously. The patterns of Chl-a [see Fig. 6(a)] and SSS [see Fig. 6(b)] in the longitude-time domain are similar qualitatively, i.e., enhanced Chl-a generally colocates with higher SSS and vice versa. The comparison of daily Chl-a and SSS demonstrates that Chl-a variation in the region is indeed in phase with SSS variation on the daily basis.

TAO measurements at 140°W and 125°W along the equator are further examined to determine whether the change of Chl-a is consistent with the change of SSS on the daily basis. Fig. 7(a) shows the changes of Chl-a and SSS in the period of March 1–December 31, 2020, at the station TAO_140W. Overall, the daily variation of Chl-a was in phase with that of SSS at this station. Except for the case before early May where there was no apparent SSS peak corresponding to the Chl-a peak, the peaks and troughs of Chl-a and SSS intuitively matched well with each other, with Chl-a and SSS ranging ∼0.15–0.35 mg/m^3 and ∼34.7–35.3 psu, respectively.

Similarly, Chl-a at station TAO_125W generally changed with SSS. Chl-a increased with the increase of SSS and vice versa, as shown in Fig. 7(b) from May 31–August 30, 2019. In this period, there were three cycles of Chl-a and SSS changes. The cycles of Chl-a variation were similar to those of SSS although some phase differences for Chl-a and SSS indeed existed. Statistical analysis shows that the cross-correlation coefficients between Chl-a and SSS are 0.77 with a time-lag of about one day at the station TAO_140W, and 0.63 with a time-lag of about two days at the station TAO_125W.

Examination of the vertical profiles of the temperature and salinity at the TAO stations [33] shows that the change of salinity could reach 20°C–24°C isotherm depth of ∼50 m. The meridional current measurements at the TAO stations in the subsurface layer were also found to contribute to the salinity changes. The vertical distributions of the temperature and salinity at 140°W along the equator reveal that the TIWs led to changes in both salinity and nutrient concentrations at the sea surface, and consequently drove the Chl-a variability from late May until late 2020.

D. Mechanism for the Synchronous Chl-a and SSS Variability

Figs. 2, 3, 5, and 7 qualitatively show the synchronous Chl-a and SSS variability in the Equatorial Pacific Ocean on the monthly basis. Chl-a and SSS anomaly patterns in Figs. 2, 3, 5, and 7 clearly show that Chl-a anomaly and SSS anomaly are highly correlated in both the daily and monthly scales. Further statistical analysis shows that along the equator between 150°E–90°W, the cross-correlation between the Chl-a ratio [see

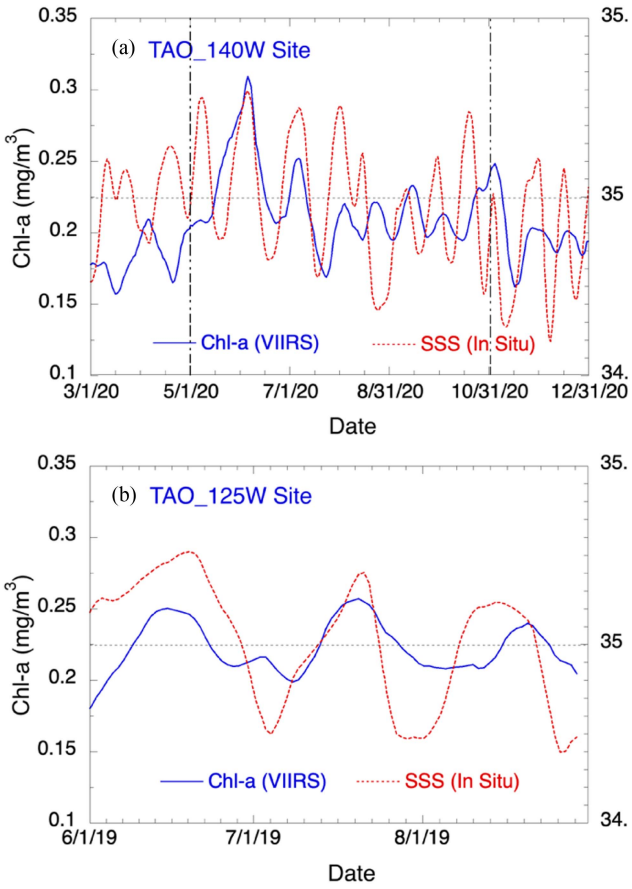

Fig. 7. Comparison of VIIRS-measured Chl-a (blue and scale noted in left) with the *in situ* SSS data (red and scale noted in right) to show their relationship in the temporal variation for the time period and location of (a) March 1–December 31, 2020, at the TAO_140W station and (b) May 31–August 30, 2019, at the TAO_125W station. Note that Chl-a and SSS are 5-day running mean values to remove the measurement noises. The time between two vertical dash lines in plot (a) marks the period with enhanced TIW activities in the Equatorial Pacific Ocean.

Fig. 5(a)] and SSS difference [see Fig. 5(b)] is 0.625. In December 2015, the cross-correlation between the Chl-a ratio and SSS difference at the equator between 150°E–90°W was 0.887, whereas it was 0.801 in August 2020.

On the daily basis, the study shows that cross-correlation coefficient with the maximum magnitude between Chl-a and SSS was 0.74 in the period between May and September 2020 at the TAO_140W station [33]. This further quantifies that Chl-a and SSS vary synchronously on the daily basis, and the TIWs are the physical driving force for the changes of Chl-a and SSS.

Chl-a dynamics in the Equatorial Pacific Ocean are related to the physical processes of the atmosphere and ocean, such as the ENSO activity and TIWs [33], [59]. Nutrients, such as nitrate and phosphate, are critical for the algal growth and phytoplankton bloom. Thus, the nutrient (nitrate, phosphate, etc.) dynamics that are driven the physical processes of the atmosphere and ocean are the major drivers for Chl-a dynamics in this region.

During the 2015 El Niño event, TAO observations (https://www.pmel.noaa.gov/tao/drupal/disdel/) exhibit that positive zonal wind anomaly colocated with both negative Chl-a and SSS anomalies, as shown in Figs. 2–4, in the Equatorial Pacific Ocean, and the spatial pattern of the positive zonal wind anomaly (results not shown) matched well with the spatial patterns of Chl-a and SSS anomalies. This suggests that Chl-a and SSS anomalies were closely related to the zonal wind anomaly. On the other hand, the spatial pattern of the SST anomaly was different from those of SSS, Chl-a, and zonal wind anomalies in terms of the location, coverage, and their extensions.

As the ocean physical property, SSS may be directly influenced by the precipitation variation. The seasonal rainfall in the equatorial region indeed leads to the seasonal change of SSS. Since SSS anomaly instead of SSS is used in this study, the seasonal effects of the precipitation variation on SSS are largely filtered out. The interannual Chl-a and SSS anomalies, as shown in Figs. 2, 3, and 5, suggest that ocean processes (e.g., equatorial upwelling, planetary waves, etc.) instead of the precipitation variation drive the changes of both SSS and nutrient levels, and consequently lead to Chl-a changes in the synoptic scale. The precipitation measurements at the TAO stations show that the precipitation is negligible after May in each year. Thus, the SSS variation after May 2020 [see Fig. 7(a)] was attributed to the ocean processes, such as equatorial upwelling, planetary waves, etc., while in early each year, the precipitation indeed can cause the SSS change and lead to inconsistency between the Chl-a and SSS changes.

On the other hand, Chl-a as a biological property can be driven by the oceanic processes, radiative forcing, etc. The similarity of the Chl-a ratio and SSS difference in Figs. 2, 3, and 5, and the inconsistency of the SST anomaly pattern [see Fig. 4(e) and (f)] and SSS difference pattern [see Figs. 2(f) and 3(f)] imply that the oceanic processes are the major force that drives the Chl-a changes, and the nutrient dynamics acts as the linkage between the synchronous Chl-a and SSS variations in the Equatorial Pacific Ocean.

The nutrient dynamics driven by the zonal wind anomaly in the western Equatorial Pacific Ocean during the 2015 El Niño was linked to depressed Chl-a and SSS. In the Equatorial Pacific Ocean, both the nutrient concentration and salinity increased with the increase of thermocline depth [60], [61]. Thus, the positive zonal wind anomaly dampened the equatorial upwelling activities and enhanced the surface water convergence in the western Equatorial Pacific Ocean, and consequently led to the anomalously low SSS and the depletion of nutrients at the sea surface. The decrease of the nutrient level further hampered algal growth and resulted in the negative Chl-a anomaly ratio in the 2015 El Niño event. The low frequency variability of Chl-a and nutrient dynamics were similar to the biological and chemical responses observed during the 1997–1998 El Niño [23]. In fact, the chemical and ecological perturbations were linked to changes in the upwelling of nutrient-enriched waters [23].

The salinity or nutrients are generally not affected by various ocean and atmospheric processes, such as solar radiation, air-sea interaction, etc., even though they are driven by the upwelling and rainfall. In comparison, SST can be significantly affected not only by wind-driven equatorial upwelling, and planetary

waves (equatorial Rossby and Kelvin waves), but also by other ocean and atmosphere processes, such as air-sea interaction, air temperature, solar radiation, etc. Thus, SSS is generally a conservative ocean property while SST is not. All these differences that drove SST, SSS, and nutrient concentration determined that the SST dynamics in the Equatorial Pacific Ocean was not synchronized with the dynamics of Chl-a, SSS, and nutrient concentration. Therefore, the spatial distribution of the SST anomaly was different from those of Chl-a and SSS as observed from VIIRS-SNPP for Chl-a and Aquarius and SMAP for SSS during the 2015 El Niño event.

Conversely, a negative zonal wind anomaly from the TAO measurements (not shown here) was observed in the western Equatorial Pacific Ocean during the 2020 La Niña event. The negative zonal wind anomaly and positive Chl-a and SSS anomalies were synchronous and colocated, as displayed in Figs. 3 and 4. This shows that the enhanced easterly trade winds led to stronger Equatorial upwelling and brought the higher nutrient and salinity waters from the subsurface layer to the sea surface, and thus triggered the algae bloom and high SSS in the western Equatorial Pacific Ocean. It is also noted that the SST anomaly was also not consistent with the Chl-a and SSS anomalies during the 2020 La Niña event (see Figs. 3 and 4). This demonstrates that the other atmospheric and ocean processes (solar radiation, air-sea interaction, etc.) also played important roles on SST variations during the La Niña event.

Even though the nutrient level is a major driver for phytoplankton growth and Chl-a variability, Chl-a can be influenced by multiple ocean, atmosphere, and biological processes. Thus, Chl-a is sensitive to a variety of ocean, atmosphere, and environmental changes. On the daily basis, the TAO observations also confirmed that Chl-a and SSS more or less covary with each other. In Fig. 7, the periodical change of SSS was driven by the westward propagating TIWs. Detailed analysis of temperature and salinity profiles across the equator from TAO observations suggests that water movement and subsurface mixing due to the TIWs can not only cause water salinity changes, but also lead to changes of the sea surface nutrient level in the Equatorial Pacific Ocean [33]. Since SSS and nutrient are highly correlated as suggested by previous studies [23], [33], the phytoplankton growth, which is represented by Chl-a concentration, was in phase with SSS on the daily basis, as shown in Fig. 7. It is also noted that there was a small time-lag between SSS peaks (troughs) and Chl-a peaks (troughs). Indeed, the cross-correlation coefficient of Chl-a and SSS at the TAO stations suggests that time-lag of Chl-a and SSS was about 1–2 days [33]. This could be attributed to the time for algal growth driven by the nutrient dynamics with the water movement and subsurface mixing in the TIWs [33]. The horizontal and vertical water movements associated with the TIWs can contribute to different time-lags. While the time-lag was short for the meridional water movement with Chl-a and SSS peaks almost in phase at the TAO_140W station [see Fig. 7(a)], it might take a longer time for the surface nutrient increase and algal growth induced by the vertical water movement and subsurface mixing due to the TIWs. Further investigations, including comprehensive *in situ* measurements for the physical, chemical, and biological properties, as well as a physical and biogeochemical modeling effort, will be necessary to fully understand the time-lag of Chl-a and SSS variations.

IV. Conclusion

As one of the most important regions that have significant impacts and implications for global climate change, the Equatorial Pacific Ocean has been extensively studied. With the advent of satellite Chl-a and SSS observations in the region, we report the synchronous Chl-a and SSS variability in the Equatorial Pacific Ocean using the 2012–2021 Chl-a data from VIIRS-SNPP and the same period SSS data from Aquarius and SMAP. This new finding reveals the linkage between the physical and biological processes in the region, and provides a better understanding about the physical, biological, and biogeochemical variabilities driven by the ENSO event.

Both Chl-a and SSS variabilities are driven by the ENSO activities. During the El Niño event, the decreased Chl-a and decreased SSS match well with each other in terms of timing and spatial coverage. Additionally, enhanced Chl-a and higher SSS match well during the La Niña event. We also found that the Chl-a and SSS anomalies are synoptically different from the SST anomaly during the El Niño and La Niña events. The mechanism that leads to the synchronized Chl-a and SSS variability, as well as why they are different from SST, has also been addressed.

Furthermore, using the TAO mooring *in situ* measurements, we show that Chl-a and SSS generally covary on the daily basis due to the propagation of the TIWs. Indeed, as a new finding of the synchronicity in Chl-a and SSS variability in the Equatorial Pacific Ocean on both the daily and monthly bases, this study not only provides new knowledge about the physical and biological processes and their interaction in the Equatorial Pacific Ocean, but also advances the understanding of the mechanism that drives the synchronization in the biological (Chl-a) and physical (SSS) variability in the region.

Acknowledgment

VIIRS global ocean color product data can be found at the NOAA Ocean Color Team website (https://www.star.nesdis.noaa.gov/sod/mecb/color/). The Aquarius and SMAP SSS data were acquired from Jet Propulsion Laboratory Physical Oceanography Distribution Active Archive Center (https://doi.org/10.5067/SMP50-3TPCS). The TAO salinity data were acquired from the NOAA Pacific Marine Environmental Laboratory (https://www.pmel.noaa.gov/gtmba/). The authors would like to thank two anonymous reviewers for their useful comments. The scientific results and conclusions, as well as any views or opinions expressed herein, are those of the author(s) and do not necessarily reflect those of NOAA or the Department of Commerce.

References

[1] H. F. Diaz, M. P. Hoerling, and J. K. Eischeid, "ENSO variability, teleconnections and climate change," *Int. J. Climatol.,* vol. 21, no. 15, pp. 1845–1862, Dec. 2001.

[2] D. Roemmich and J. Gilson, "The global ocean imprint of ENSO," *Geo-Phys. Res. Lett.,* vol. 38, no. 13, Jul. 2011, Art. no. L13606, doi: 10.1029/2011gl047992.

[3] P. B. Wright, "Relationships between indexes of the southern oscillation," *Monthly Weather Rev.,* vol. 112, no. 9, pp. 1913–1919, 1984, doi: 10.1175/1520-0493112.

[4] S. W. Yeh, J. S. Kug, B. Dewitte, M. H. Kwon, B. P. Kirtman, and F. F. Jin, "El Niño in a changing climate," *Nature,* vol. 461, no. 7263, pp. 511–514, Sep. 2009, doi: 10.1038/nature08316.

[5] M. J. McPhaden, S. E. Zebiak, and M. H. Glantz, "ENSO as an integrating concept in earth science," *Science,* vol. 314, no. 5806, pp. 1740–1745, Dec. 2006, doi: 10.1126/science.1132588.

[6] S. G. H. Philander, "El-Niño and La-Niña," *J. Atmos. Sci.,* vol. 42, no. 23, pp. 2652–2662, Dec. 1985, doi: 10.1175/1520-0469042.

[7] K. Fraedrich and K. Muller, "Climate anomalies in Europe associated with ENSO extremes," *Int. J. Climatol.,* vol. 12, no. 1, pp. 25–31, Jan./Feb. 1992.

[8] K. Fraedrich, "An ENSO impact on Europe—A review," *Tellus Ser. A-Dyn. Meteorol. Oceanogr.*, vol. 46, no. 4, pp. 541–552, Aug. 1994, doi: 10.1034/j.1600-0870.1994.00015.

[9] S. D. Schubert, Y. Chang, M. J. Suarez, and P. J. Pegion, "ENSO and wintertime extreme precipitation events over the contiguous United States," *J. Climate,* vol. 21, no. 1, pp. 22–39, Jan. 2008, doi: 10.1175/2007jcli1705.1.

[10] C. D. Jones, M. Collins, P. M. Cox, and S. A. Spall, "The carbon cycle response to ENSO: A coupled climate-carbon cycle model study," *J. Climate,* vol. 14, no. 21, pp. 4113–4129, 2001.

[11] S. W. Park, J. S. Kim, J. S. Kug, M. F. Stuecker, I. W. Kim, and M. Williams, "Two aspects of decadal ENSO variability modulating the long-term global carbon cycle," *Geo-Phys. Res. Lett.,* vol. 47, no. 8, Apr. 2020, Art. no. e2019GL086390, doi: 10.1029/2019GL086390.

[12] J. S. Kim, J. S. Kug, and S. J. Jeong, "Intensification of terrestrial carbon cycle related to El Niño-Southern Oscillation under greenhouse warming," *Nature Commun.,* vol. 8, 2017, Art. no. 1674, doi: 10.1038/s41467-017-02461-9.

[13] M. Holmgren, M. Scheffer, E. Ezcurra, J. R. Gutierrez, and G. M. J. Mohren, "El Niño effects on the dynamics of terrestrial ecosystems," *Trends Ecol. Evol.*, vol. 16, no. 2, pp. 89–94, Feb. 2001.

[14] P. Lehodey, "The pelagic ecosystem of the tropical Pacific Ocean: Dynamic spatial modelling and biological consequences of ENSO," *Prog. Oceanogr.*, vol. 49, no. 1–4, pp. 439–468, 2001, doi: 10.1016/S0079-6611(01)00035-0.

[15] D. M. Karl et al., "Ecosystem changes in the North Pacific subtropical gyre attributed to the 1991-92 El-Niño," *Nature,* vol. 373, no. 6511, pp. 230–234, Jan. 1995.

[16] J. W. Hansen, A. W. Hodges, and J. W. Jones, "ENSO influences on agriculture in the southeastern United States," *J. Climate,* vol. 11, no. 3, pp. 404–411, Mar. 1998.

[17] C. C. Chen and B. A. McCarl, "The value of ENSO information to agriculture: Consideration of event strength and trade," *J. Agricultural Resour. Econ.,* vol. 25, no. 2, pp. 368–385, Dec. 2000.

[18] M. Dilley and B. N. Heyman, "ENSO and disaster: Droughts, floods and El Niño/Southern Oscillation warm events," *Disasters,* vol. 19, no. 3, pp. 181–193, Sep. 1995, doi: 10.1111/j.1467-7717.1995.tb00338.x.

[19] J. Y. Park, J. S. Kug, J. Park, S. W. Yeh, and C. J. Jang, "Variability of chlorophyll associated with El Niño-Southern Oscillation and its possible biological feedback in the equatorial Pacific," *J. Geo-Phys. Res. Oceans,* vol. 116, no. C10, Oct. 2011, doi: 10.1029/2011jc007056.

[20] S. Ferrett and M. Collins, "ENSO feedbacks and their relationships with the mean state in a flux adjusted ensemble," *Climate Dyn.,* vol. 52, no. 12, pp. 7189–7208, Jun. 2019, doi: 10.1007/s00382-016-3270-9.

[21] M. F. Racault, S. Sathyendranath, R. J. W. Brewin, D. E. Raitsos, T. Jackson, and T. Platt, "Impact of El Niño variability on Oceanic phytoplankton," *Frontier Mar. Sci.,* vol. 4, 2017, Art. no. 133, doi: 10.3389/fmars.00133.

[22] M. J. Behrenfeld et al., "Biospheric primary production during an ENSO transition," *Science,* vol. 291, no. 5513, pp. 2594–2597, Mar. 2001.

[23] F. P. Chavez et al., "Biological and chemical response of the equatorial Pacific Ocean to the 1997-98 El Niño," *Science*, vol. 286, no. 5447, pp. 2126–2131, Dec. 1999.

[24] F. P. Chavez, P. G. Strutton, and M. J. McPhaden, "Biological-physical coupling in the central equatorial Pacific during the onset of the 1997–98 El Niño," *Geo-Phys. Res. Lett.*, vol. 25, no. 19, pp. 3543–3546, Oct. 1998.

[25] P. K. Dunstan et al., "Global patterns of change and variation in sea surface temperature and chlorophyll a," *Sci. Rep.,* vol. 8, Oct. 2018, Art. no. 14624, doi: 10.1038/s41598-018-33057-y.

[26] W. Shi and M. Wang, "Satellite-observed biological variability in the equatorial Pacific during the 2009-2011 ENSO cycle," *Adv. Space Res.,* vol. 54, no. 9, pp. 1913–1923, Nov. 2014, doi: 10.1016/j.asr.2014.07.003.

[27] J. F. Qi et al., "Salinity variability in the tropical Pacific during the Central-Pacific and Eastern-Pacific El Niño events," *J. Mar. Syst.,* vol. 199, Nov. 2019, Art. no. 103225, doi: 10.1016/j.jmarsys.2019.103225.

[28] S. Cravatte, T. Delcroix, D. X. Zhang, M. McPhaden, and J. Leloup, "Observed freshening and warming of the western Pacific warm pool," *Climate Dyn.,* vol. 33, no. 4, pp. 565–589, Sep. 2009, doi: 10.1007/s00382-009-0526-7.

[29] A. Singh, T. Delcroix, and S. Cravatte, "Contrasting the flavors of El Niño-Southern Oscillation using sea surface salinity observations," *J. Geo-Phys. Res. Oceans,* vol. 116, Jun. 2011, doi: 10.1029/2010jc006862.

[30] C. M. Corbett, B. Subrahmanyam, and B. S. Giese, "A comparison of sea surface salinity in the equatorial Pacific Ocean during the 1997-1998, 2012-2013, and 2014-2015 ENSO events," *Climate Dyn.,* vol. 49, no. 9/10, pp. 3513–3526, Nov. 2017, doi: 10.1007/s00382-017-3527-y.

[31] J. Chi, Y. Du, Y. Zhang, X. Nie, P. Shi, and T. Qu, "A new perspective of the 2014/15 failed El Niño as seen from ocean salinity," *Sci. Rep.,* vol. 9, Feb. 2019, Art. no. 2720, doi: 10.1038/s41598-019-38743-z.

[32] C. Guan, F. Tian, M. J. McPhaden, F. Wang, S. J. Hu, and R. H. Zhang, "Zonal structure of tropical Pacific surface salinity anomalies affects ENSO intensity and asymmetry," *Geo-Phys. Res. Lett.,* vol. 49, no. 1, Jan. 2022, Art. no. e2021GL096197, doi: 10.1029/2021GL096197.

[33] W. Shi and M. Wang, "Tropical instability wave modulation of chlorophyll-a in the Equatorial Pacific," *Sci. Rep.,* vol. 11, no. 1, Nov. 2021, Art. no. 22517, doi: 10.1038/s41598-021-01880-5.

[34] T. Lee, G. Lagerloef, M. M. Gierach, H. Y. Kao, S. Yueh, and K. Dohan, "Aquarius reveals salinity structure of tropical instability waves," *Geo-Phys. Res. Lett.,* vol. 39, Jun. 2012, doi: 10.1029/2012gl052232.

[35] A. Hasson, M. Puy, J. Boutin, E. Guilyardi, and R. Morrow, "Northward pathway across the tropical North Pacific Ocean revealed by surface salinity: How do El Niño anomalies reach Hawaii?," *J. Geo-Phys. Res. Oceans,* vol. 123, no. 4, pp. 2697–2715, Apr. 2018, doi: 10.1002/2017jc013423.

[36] A. Hasson, T. Delcroix, J. Boutin, R. Dussin, and J. Ballabrera-Poy, "Analyzing the 2010-2011 La Niña signature in the tropical Pacific sea surface salinity using *in situ* data, SMOS observations, and a numerical simulation," *J. Geo-Phys. Res. Oceans,* vol. 119, no. 6, pp. 3855–3867, Jun. 2014, doi: 10.1002/2013jc009388.

[37] E. C. Hackert, R. M. Kovach, A. J. Busalacchi, and J. Ballabrera-Poy, "Impact of Aquarius and SMAP satellite sea surface salinity observations on coupled El Niño/Southern Oscillation forecasts," *J. Geo-Phys. Res. Oceans,* vol. 124, no. 7, pp. 4546–4556, Jul. 2019, doi: 10.1029/2019jc015130.

[38] E. Hackert et al., "Satellite sea surface salinity observations impact on El Niño/Southern Oscillation predictions: Case studies from the NASA GEOS seasonal forecast system," *J. Geo-Phys. Res. Oceans,* vol. 125, no. 4, Apr. 2020, Art. no. e2019JC015788, doi: 10.1029/2019JC015788.

[39] X. B. Yin, J. Boutin, G. Reverdin, T. Lee, S. Arnault, and N. Martin, "SMOS sea surface salinity signals of tropical instability waves," *J. Geo-Phys. Res. Oceans,* vol. 119, no. 11, pp. 7811–7826, Nov. 2014, doi: 10.1002/2014jc009960.

[40] X. Liu and M. Wang, "Gap filling of missing data for VIIRS global ocean color products using the DINEOF method," *IEEE Trans. Geosci. Remote Sens.*, vol. 56, no. 8, pp. 4464–4476, Aug. 2018, doi: 10.1109/Tgrs.2018.2820423.

[41] X. Liu and M. Wang, "Filling the gaps of missing data in the merged VIIRS SNPP/NOAA-20 ocean color product using the DINEOF method," *Remote Sens.,* vol. 11, no. 2, Jan. 2019, Art. no. 178, doi: 10.3390/rs11020178.

[42] X. Liu and M. Wang, "Global daily gap-free ocean color products from multi-satellite measurements," *Int. J. Appl. Earth Observ. Geo-Inf.,* vol. 108, Apr. 2022, Art. no. 102714, doi: 10.1016/j.jag.2022.102714.

[43] C. R. McClain, "A decade of satellite ocean color observations," *Annu. Rev. Mar. Sci.,* vol. 1, pp. 19–42, 2009, doi: 10.1146/annurev.marine.010908.163650.

[44] W. E. Esaias et al., "An overview of MODIS capabilities for ocean science observations," *IEEE Trans. Geosci. Remote Sens.,* vol. 36, no. 4, pp. 1250–1265, Jul. 1998, doi: 10.1109/36.701076.

[45] K. Mikelsons, M. Wang, and L. Jiang, "Statistical evaluation of satellite ocean color data retrievals," *Remote Sens. Environ.,* vol. 237, Feb. 2020, Art. no. 111601, doi: 10.1016/j.rse.2019.111601.

[46] M. Wang et al., "Impacts of VIIRS SDR performance on ocean color products," *J. Geo-Phys. Res. Atmos.,* vol. 118, no. 18, pp. 10347–10360, Sep. 2013, doi: 10.1002/Jgrd.50793.

[47] M. Wang and S. Son, "VIIRS-derived chlorophyll-a using the ocean color index method," *Remote Sens. Environ.,* vol. 182, pp. 141–149, Sep. 2016, doi: 10.1016/j.rse.2016.05.001.

[48] K. Mikelsons and M. Wang, "Optimal satellite orbit configuration for global ocean color product coverage," *Opt. Express,* vol. 27, no. 8, pp. A445–A457, Apr. 2019, doi: 10.1364/Oe.27.00a445.

[49] D. M. Le Vine, G. S. E. Lagerloef, F. R. Colomb, S. H. Yueh, and F. A. Pellerano, "Aquarius: An instrument to monitor sea surface salinity from space," *IEEE Trans. Geosci. Remote Sens.,* vol. 45, no. 7, pp. 2040–2050, Jul. 2007, doi: 10.1109/Tgrs.2007.898092.

[50] H. Y. Kao, G. S. E. Lagerloef, T. Lee, O. Melnichenko, T. Meissner, and P. Hacker, "Assessment of Aquarius sea surface salinity," *Remote Sens.,* vol. 10, no. 9, Sep. 2018, Art. no. 1341, doi: 10.3390/rs10091341.

[51] P. O'Neill, D. Entekhabi, E. Njoku, and K. Kellogg, "The NASA soil moisture active passive (SMAP) mission: Overview," in *Proc. IEEE Int. Geosci. Remote Sens. Symp.*, 2010, pp. 3236–3239, doi: 10.1109/Igarss.5652291.

[52] S. K. Chan et al., "Assessment of the SMAP passive soil moisture product," *IEEE Trans. Geosci. Remote Sens.,* vol. 54, no. 8, pp. 4994–5007, Aug. 2016, doi: 10.1109/Tgrs.2016.2561938.

[53] A. G. Fore, S. H. Yueh, W. Tang, B. Stiles, and A. K. Hayashi, "Combined active/passive retrievals of ocean vector wind and sea surface salinity with SMAP," *IEEE Trans. Geosci. Remote Sens.,* vol. 54, no. 12, pp. 7396–7404, Dec. 2016, doi: 10.1109/Tgrs.2016.2601486.

[54] W. Q. Tang et al., "Validating SMAP SSS with in situ measurements," *Remote Sens. Environ.,* vol. 200, pp. 326–340, Oct. 2017, doi: 10.1016/j.rse.2017.08.021.

[55] M. J. McPhaden et al., "The tropical ocean global atmosphere observing system: A decade of progress," *J. Geo-Phys. Res. Oceans,* vol. 103, no. C7, pp. 14169–14240, Jun. 1998, doi: 10.1029/97jc02906.

[56] K. Wolter, "The Southern Oscillation in surface circulation and climate over the tropical Atlantic, Eastern Pacific, and Indian Oceans as captured by cluster-analysis," *J. Climate Appl. Meteorol.,* vol. 26, no. 4, pp. 540–558, Apr. 1987, doi: 10.1175/1520-04500262.

[57] K. Wolter and M. S. Timlin, "El Niño/Southern Oscillation behaviour since 1871 as diagnosed in an extended multivariate ENSO index (MEI. ext)," *Int. J. Climatol.,* vol. 31, no. 7, pp. 1074–1087, Jun. 2011, doi: 10.1002/Joc.2336.

[58] M. Wang, L. D. Jiang, K. Mikelsons, and X. M. Liu, "Satellite-derived global chlorophyll-a anomaly products," *Int. J. Appl. Earth Observ. Geo-Inf.,* vol. 97, May 2021, Art. no. 102288, doi: 10.1016/j.jag.2020.102288.

[59] R. Legeckis, "Long waves in the eastern equatorial Pacific Ocean: A view from a geostationary satellite," *Science,* vol. 197, no. 4309, pp. 1179–1181, 1977, doi: 10.1126/science.197.4309.1179.

[60] H. Garcia et al., *World Ocean Atlas: Dissolved Inorganic Nutrients (Phosphate, Nitrate and Nitrate+Nitrite, Silicate)*, vol. 4. Silver Spring, MD, USA: NOAA Atlas NESDIS, 2018, 842019.

[61] M. M. Zweng et al., *World Ocean Atlas: Salinity*, vol. 2. Silver Spring, MD, USA: NOAA Atlas NESDIS, 2018, 822018.